Effective Surface Plasmon Polaritons Induced by Modal Dispersion in a Waveguide

Zhuo Li,[1,3,*] Liangliang Liu,[1] Hengyi Sun,[1] Yunhe Sun,[1] Changqing Gu,[1] Xinlei Chen,[1] Yun Liu,[1] and Yu Luo[2,†]
[1]*Key Laboratory of Radar Imaging and Microwave Photonics, Ministry of Education,*
College of Electronic and Information Engineering, Nanjing University of Aeronautics and Astronautics,
Nanjing 211106, People's Republic of China
[2]*School of Electrical and Electronic Engineering, Nanyang Technological University,*
Nanyang Avenue 639798, Singapore
[3]*State Key Laboratory of Millimeter Waves, Southeast University, Nanjing 210096,*
People's Republic of China

(Received 2 January 2017; revised manuscript received 16 March 2017; published 27 April 2017)

We provide further theoretical insights and experimental verification of the modal-dispersion-induced effective surface-plasmon polaritons (ESPPs) by engineering the transverse-electric (TE) modes in conventional rectangular waveguides. The complete field distributions, dispersion relations, and asymptotic frequency of the ESPPs are derived analytically. Wave-port excitations and smooth bridges are designed for the mode conversion between propagating modes in rectangular waveguides and the ESPPs. Analytical calculations and numerical simulations are performed for TE_{10}- and TE_{20}-mode-induced ESPPs, showing excellent agreement. Moreover, we design a double-layered substrate-integrated waveguide showing that ESPPs are supported at the interface between the two layers with different dielectric constants. This work opens up an avenue for low-frequency designer surface plasmons and may find potential applications in the design of compact filters, resonators, and sensors of ESPPs in the microwave and terahertz frequencies.

DOI: 10.1103/PhysRevApplied.7.044028

I. INTRODUCTION

Plasmonics reveals how electromagnetic fields can be confined and manipulated on subwavelength scales [1–9]. The interactions between photons and conduction electrons at metal-dielectric interfaces or in small metallic nanostructures lead to significant enhancement of the optical near field at the subwavelength regime. Surface-plasmon polaritons (SPPs) and localized surface plasmons (LSPs) are the two ingredients of plasmonics. They were investigated as early as 1900 and developed throughout the 20th century with a steady flow of exciting phenomena and promising applications, including miniaturization of photonic circuits in terms of SPPs- and LSPs-based near-field optics, surface-enhanced spectroscopy, plasmonic antennas, photovoltaics, etc. [1]. SPPs and LSPs occur only at the interface between two materials whose real parts of permittivity functions have opposite values at operating wavelengths, for instance, the metal-dielectric interface at optical frequencies. However, large dissipative losses severely limit the performance of metal-based plasmonic devices at optical frequencies. At lower frequencies (far infrared, terahertz, or microwave), metals behave akin to perfect electric conductors (PECs), which do not support surface plasmons. In 2004, Pendry *et al.* [10] proposed the concept of spoof surface plasmons to mimic the exciting properties of surface plasmons at low frequencies by decorating the metal surface with periodic subwavelength grooves or holes. Later, in 2012, Garcia-Vidal *et al.* [11] demonstrated that periodically textured PEC particles in two and three dimensions can support spoof localized surface plasmons (spoof LSPs). These two works set up the basis for transferring the exotic features of SPPs and LSPs to lower frequencies and aroused a series of efforts to realize low-frequency plasmonics as well as its applications [12–28]. Hybrid Airy plasmons were revealed by taking a hybrid graphene-based plasmonic waveguide in the terahertz regime [29]. The calculation and demonstration of the spatiotemporal dynamics of two-dimensional plasmon generation in graphene showed how a swift electron generates plasmons in space and time [30]. Recently, Engheta *et al.* [31] proposed an alternative methodology to realize a variety of plasmonic phenomena by exploiting modal dispersion of electromagnetic modes in bounded waveguides filled with materials of positive permittivity only. The phenomena of surface-plasmon polaritons, localized plasmonic resonance, plasmonic cloaking, and epsilon-near-zero-based tunneling have been clearly realized and numerically demonstrated by tuning the effective permittivity of the transverse-electric (TE) mode in a parallel-plate waveguide and rectangular waveguide. These modal-dispersion-induced effective surface-plasmon polaritons (ESPPs) are different from conventional spoof surface-plasmon polaritons because the ESPPs are not generated by the corrugations of metallic structures.

Although previous work [31] realized several optical functions using plasmonics without negative dielectrics, the

---

[*] lizhuo@nuaa.edu.cn
[†] luoyu@ntu.edu.sg

existence of the modal-dispersion-induced ESPPs has not been verified through experiments. In this work, we explicitly investigate the physical mechanism behind the ESPPs and show that the dispersion relations can be effectively tuned by the thickness and permittivity of each dielectric layer as well as the distance between two metal wires. Furthermore, we extend the theory to other possible modes in rectangular waveguides, in which a series of modes whose electric and magnetic lines of force satisfy the requirements of natural SPPs can be utilized to realize ESPPs. We derive a generalized analytical formula of the effective permittivity, which depends on the geometric dimensions of the guided-wave structure, filling materials, and the operating frequency. In addition, the electromagnetic field distributions and dispersion relations of the modal-dispersion-induced ESPPs are derived analytically, which provide useful guidance in the design of smooth bridges for the mode conversion between conventional modes in rectangular waveguides and the ESPPs. Two specific examples of the TE_{10}^z- and TE_{20}^z-mode-induced ESPPs are investigated with excellent agreement between the theory and simulations. Finally, a double-layered substrate-integrated waveguide (SIW) is designed to realize the transmission of ESPPs at the interface between two dielectrics with distinct permittivities. Simulation and experimental results verify the existence of the ESPPs.

II. THEORY AND DISCUSSION: MODAL-DISPERSION-INDUCED EFFECTIVE SPPs IN THE RECTANGULAR WAVEGUIDE

We first revisit the geometry of a conventional rectangular waveguide shown in Fig. 1, assuming that it is filled with double-layered isotropic and homogeneous dielectrics of relative permittivities ε_{r1} and ε_{r2} and relative permeabilities $\mu_{r1} = 1$ and $\mu_{r2} = 1$ in the bottom $-(b-t) < y < 0$ and upper $0 < y < t$ regions. Normally, a rectangular waveguide supports both TE and transverse magnetic (TM) modes propagating along the z direction if both dielectrics have positive permittivity. Surface modes are supported at the boundary of two materials if the real parts of ε_{r1} and ε_{r2} have opposite signs. Therefore, it seems impossible to have SPPs propagation on positive dielectrics. Thanks to the idea of Engheta that a natural positive dielectric can be viewed as an effective negative one for a desired mode in a bounded waveguide induced by modal dispersion, we show through analytical derivations that it is possible to realize the modal-dispersion-induced confined surface mode (called ESPPs in this paper) at this interface within a certain frequency regime. From the effective-medium aspect, the relative permittivities ε_{r1} and ε_{r2} can be replaced by their effective counterparts ε_{e1} and ε_{e2} for a certain mode, which can be tuned to mimic real metals and dielectrics in optical frequencies. Additionally, it is convenient to realize mode conversion between the $\mathrm{TE}_{m0}^z (m = 1, 2, \ldots)$ modes and the ESPPs through a mode transition structure that can achieve gradient and smooth variations of the wave momentum.

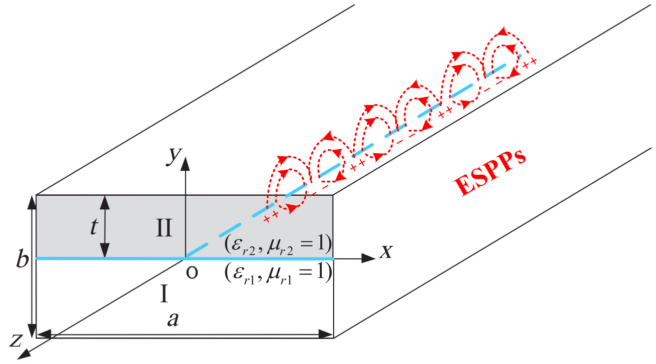

FIG. 1. A conventional rectangular waveguide with the cross-section dimensions $a \times b$ filled with double-layered isotropic and homogeneous dielectrics with relative permittivities ε_{r1} and ε_{r2} and relative permeabilities $\mu_{r1} = 1$ and $\mu_{r2} = 1$. The interface (denoted as the solid blue line) between them is supposed to support modal-dispersion-induced ESPPs transmitted along the z direction.

Let us begin by revisiting the propagation constant of the TE_{m0}^z modes in a dielectric-filled waveguide $k_z = \sqrt{k^2 - k_c^2} = \sqrt{k^2 - [(m\pi)/a]^2}$, in which $k = k_0\sqrt{\varepsilon_r}$ is the wave number in the dielectric with relative permittivity ε_r, $k_c = [(m\pi)/a]$ is the cutoff wave number in the x direction, and m denotes the half-wavelength number along the x direction. When $k > k_c$, k_z is real, indicating that these TE_{m0}^z modes are propagating modes in the waveguide. If we define the relative permittivity of the effective dielectric filling in the waveguide corresponding to a specified TE_{m0}^z mode as $\varepsilon_e = \varepsilon_r - \{[(m/a)^2]/4\}\lambda_0^2$ (λ_0 is the operating wavelength), the effective wave number in the effective dielectric will be $k_e = k_0\sqrt{\varepsilon_e}$, and the effective mode will have no variations in the x direction considering that the variations of the original fields in the x direction are equivalent into the effective permittivity. Thus, it is possible to realize effective surface-confined modes supported at the interface between two effective dielectrics with permittivities of opposite signs in their real parts $[\mathrm{Re}(\varepsilon_{e1})\mathrm{Re}(\varepsilon_{e2}) < 0]$, in which $\varepsilon_{ei} = \varepsilon_{ri} - \{[(m/a)^2]/4\}\lambda_0^2$, $i = 1, 2$. Then, we set the magnetic vector potential for the effective modes in region II in Fig. 1 in the form of

$$\vec{A}_2 = \hat{y}\psi_2, \qquad \psi_2 = e^{-j\beta z}(B_2 e^{-k_{2y}y} + C_2 e^{k_{2y}y})$$

with no variations in the x direction, in which B_2 and C_2 are the amplitudes of the decaying fields from the interface into region II and the reflected fields bouncing back from the upper wall. $k_{2y} = \sqrt{\beta^2 - (k_{2e})^2}$ is the wave number in the y direction, in which $k_{2e} = k_0\sqrt{\varepsilon_{e2}}$ is the wave number in the effective dielectric of region II. Thus, we can derive all components of the electric and magnetic fields in region II according to $\vec{E} = -j\omega\vec{A} - j[1/(\omega\mu\varepsilon)]\nabla(\nabla \cdot \vec{A})$ and $\vec{H} = (1/\mu)\nabla \times \vec{A}$ as follows:

$$H_x{}^{\mathrm{II}} = \frac{j\beta}{\mu_0} e^{-j\beta z}(B_2 e^{-k_{2y}y} + C_2 e^{k_{2y}y}),$$
$$E_y{}^{\mathrm{II}} = -j\frac{1}{\omega\mu_0\varepsilon_0\varepsilon_{e2}}(k_2^2 + k_{2y}^2)e^{-j\beta z}(B_2 e^{-k_{2y}y} + C_2 e^{k_{2y}y}),$$
$$E_z{}^{\mathrm{II}} = -\frac{\beta k_{2y}}{\omega\mu_0\varepsilon_0\varepsilon_{e2}} e^{-j\beta z}(-B_2 e^{-k_{2y}y} + C_2 e^{k_{2y}y}).$$

In the same manner, we set the magnetic vector potential in region I in the form of

$$\vec{A}_1 = \hat{y}\psi_1, \qquad \psi_1 = e^{-j\beta z}(B_1 e^{k_{1y}y} + C_1 e^{-k_{1y}y})$$

with no variations in the x direction, in which B_1 and C_1 are the amplitudes of the decaying fields from the interface into region I and the reflected fields bouncing back from the lower wall. $k_{1y} = \sqrt{\beta^2 - (k_{1e})^2}$ is the wave number in the y direction, in which $k_{1e} = k_0\sqrt{\varepsilon_{e1}}$ is the wave number in the effective dielectric of region I. Thus, from Maxwell's equations we can derive all components of the electric and magnetic fields in region I as follows:

$$H_x{}^{\mathrm{I}} = \frac{j\beta}{\mu_0} e^{-j\beta z}(B_1 e^{k_{1y}y} + C_1 e^{-k_{1y}y}),$$
$$E_y{}^{\mathrm{I}} = -j\frac{1}{\omega\mu_0\varepsilon_0\varepsilon_{e1}}(k_1^2 + k_{1y}^2)e^{-j\beta z}(B_1 e^{k_{1y}y} + C_1 e^{-k_{1y}y}),$$
$$E_z{}^{\mathrm{I}} = -\frac{\beta k_{1y}}{\omega\mu_0\varepsilon_0\varepsilon_{e1}} e^{-j\beta z}(B_1 e^{k_{1y}y} - C_1 e^{-k_{1y}y}).$$

By imposing the following boundary conditions at the interface ($y = 0$) and the two conducting walls [$y = t$ and $y = -(b - t)$] where

$$\begin{aligned}
&y = 0,\\
&E_z{}^{\mathrm{II}} = E_z{}^{\mathrm{I}} \Rightarrow k_{2y}\varepsilon_{e1}(B_2 - C_2) = -k_{1y}\varepsilon_{e2}(B_1 - C_1),\\
&y = 0, \quad H_x{}^{\mathrm{II}} = H_x{}^{\mathrm{I}} \Rightarrow B_2 + C_2 = B_1 + C_1,\\
&y = t, \quad E_z{}^{\mathrm{II}} = 0 \Rightarrow B_2 e^{-k_{2y}t} = C_2 e^{k_{2y}t},\\
&y = -(b - t),\\
&E_z{}^{\mathrm{I}}[-(b - t)] = 0 \Rightarrow B_1 e^{-k_{1y}(b-t)} = C_1 e^{k_{1y}(b-t)},
\end{aligned}$$

we can obtain the dispersion relation for modal-dispersion-induced ESPPs as

$$k_{2y}\varepsilon_{e1}\tanh(k_{2y}t) = -k_{1y}\varepsilon_{e2}\tanh[k_{1y}(b - t)]. \tag{1}$$

This expression is valid for both real and complex ε_{e1} and ε_{e2}, i.e., for dielectrics without and with losses. It can be observed from the above dispersion relation that for the surface-confined modes [$\mathrm{Re}(k_{1y}) > 0$ and $\mathrm{Re}(k_{2y}) > 0$], ε_{e1} and ε_{e2} must have opposite sign in their real parts, which can be realized by tuning the operating frequency, geometric dimensions of the waveguide, and filling materials for a certain TE_{m0}^{z} mode. Assuming $\mathrm{Re}(\varepsilon_{r2}) > \mathrm{Re}(\varepsilon_{r1})$ without losing generality, it is imperative that $\mathrm{Re}(\varepsilon_{e1}) < 0$ and $\mathrm{Re}(\varepsilon_{e2}) > 0$ for this interface to support the modal-dispersion-induced ESPPs, which requires that the working frequency $\omega_0 = 2\pi f_0$ of the ESPPs must be higher than $\omega_2 = \omega_{\mathrm{cutoff}}|_{\mathrm{TE}m0,\varepsilon_{r2}} = \{\pi c/[\sqrt{\mathrm{Re}(\varepsilon_{r2})}]\}(m/a)$, in which ω_2 is the cutoff frequency of the TE_{m0}^{z} mode in a conventional rectangular waveguide filled with the dielectric of relative permittivity ε_{r2}. According to the dispersion relations, we can obtain the evolution of the dispersion curves with the variations of the thickness t of region II for specified ε_{r1} and ε_{r2}. By a close examination of the group velocity $d\omega/d\beta$ on the dispersion curve for the ESPPs with the variations of t, we find that when $0 < t \leq b/2$, the group velocity is always positive until $\beta \to \infty$, where the frequency approaches the asymptotic frequency $\omega_{\mathrm{SP}} = \pi c\sqrt{\{2/[\mathrm{Re}(\varepsilon_{r1} + \varepsilon_{r2})]\}}(m/a)$, which is the characteristic surface-plasmon frequency of the SPPs that are supported at the interface between two semi-infinite dielectrics with permittivities ε_{e1} and ε_{e2}. However, when $b/2 < t < b$, the group velocity is first positive with the increase of β and becomes negative after a peak where the group velocity is zero. We can easily find the exact peak (β_p, ω_p) for each curve by $d\omega/d\beta = 0$. When $\beta > \beta_p$, the frequency of each dispersion curve decreases and also approaches the asymptotic frequency ω_{SP} when $\beta \to \infty$. Thus, if ε_{r1}, ε_{r2}, a, b, and m are all fixed, the working bandwidth of the ESPPs must be $\omega_2 < \omega_0 < \omega_{\mathrm{SP}}$ when $0 < t \leq b/2$ and $\omega_2 < \omega_0 < \omega_p$ when $b/2 < t < b$. For a specific case when only the dominant TE_{10}^{z} mode ($m = 1$, $n = 0$) is excited in an X-band rectangular waveguide and if we focus only on designing an interface between air ($\varepsilon_{r1} = 1$) and a lossless dielectric with the relative permittivity ($\varepsilon_{2r} = 4$), the dispersion relation for the TE_{10}^{z} modal-dispersion-induced ESPPs at the interface can be obtained analytically as

$$\begin{aligned}
&\left[\omega^2 - c^2\left(\frac{\pi}{a}\right)\right]\sqrt{\beta^2 + \left(\frac{\pi}{a}\right)^2 - 4k_0^2}\\
&\quad\times\tanh\left[t\sqrt{\beta^2 + \left(\frac{\pi}{a}\right)^2 - 4k_0^2}\right]\\
&= -\left[4\omega^2 - c^2\left(\frac{\pi}{a}\right)^2\right]\sqrt{\beta^2 + \left(\frac{\pi}{a}\right)^2 - k_0^2}\\
&\quad\times\tanh\left[(b - t)\sqrt{\beta^2 + \left(\frac{\pi}{a}\right)^2 - k_0^2}\right].
\end{aligned} \tag{2}$$

The evolution of the dispersion relations with the variations of t is obtained by solving the transcendental equation, Eq. (2), numerically and drawn in Fig. 2(a). When $t = b$, the dashed black line in Fig. 2(a) corresponds to the dispersion curve of the TE_{10}^{z} mode in a rectangular

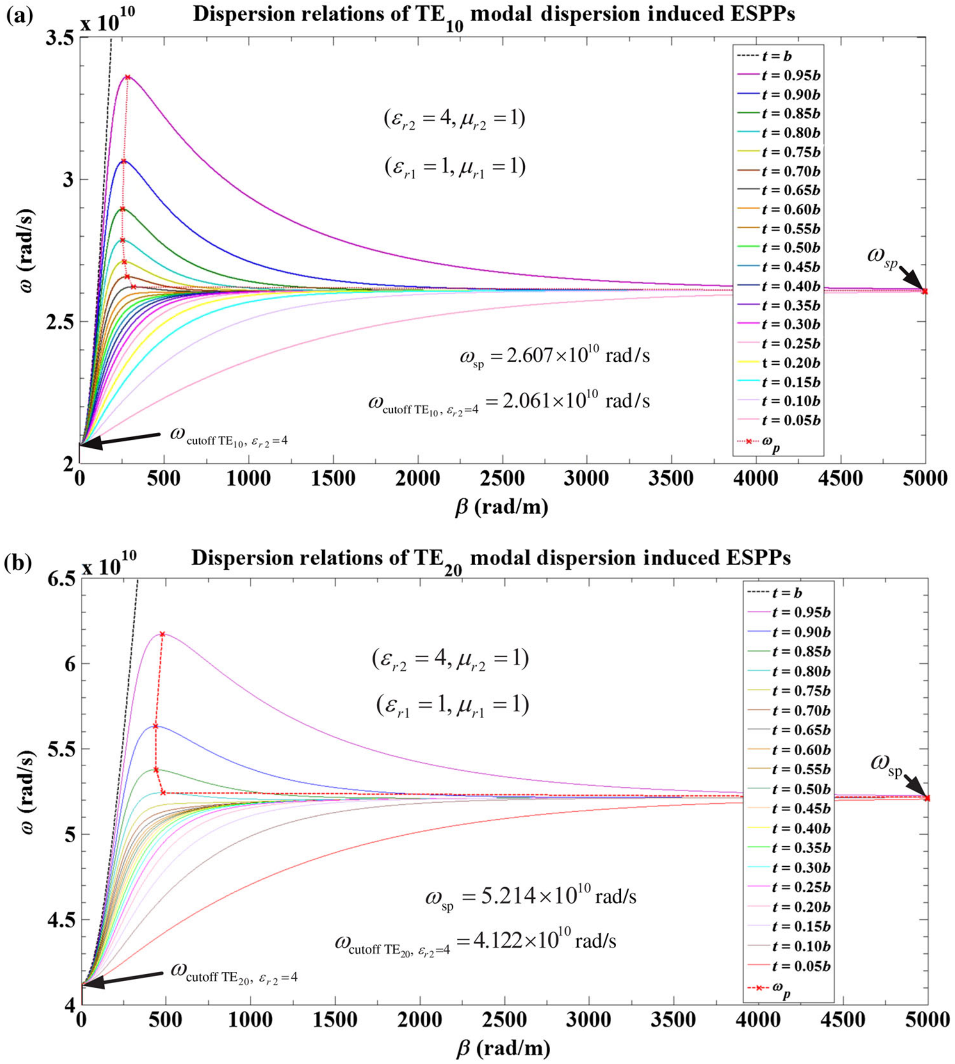

FIG. 2. Evolution of the dispersion curves of the TE modal-dispersion-induced ESPPs in a standard X-band rectangular waveguide (WR90, $a \times b = 22.86 \times 10.16\ \mathrm{mm}^2$) with the variations of the dielectric thickness $t = 0.05b \sim b$ with a step of $0.05b$. (a) TE_{10} case. (b) TE_{20} case.

waveguide purely filled with the dielectric with the relative permittivity $\varepsilon_{r2} = 4$. With the decrease of t, the dispersion curves deviate away from the dashed line, exhibiting surface-confined characteristics at the interface. As we state above, when $b/2 < t < b$, this surface mode has negative group velocity after a peak with the trajectory denoted by the dotted red line. If we set $t = b/2$, the ESPPs spectrum can be obtained as $[\pi c/(2a)] = \omega_{\text{cutoff TE}_{10},\varepsilon_{r2}=4} < \omega_0 < \omega_{\text{SP}} = [2\pi c/(\sqrt{10}a)]$. We can observe that the dispersion curves deviate more from the dotted black line with the decrease of t, which gives us a bonus on how to smoothly convert the TE_{10}^z mode in a purely dielectric filled waveguide to the ESPPs at the dielectric-air interface between two equal-thickness layers simply by changing the thickness t from $t = b$ to $t = b/2$ continuously. In previous work, Engheta *et al.* [31] placed a series of thin metallic wires along the entire interface between an effective-double-positive-media and effective-epsilon-negative-media layer inside a parallel-plate waveguide to support the ESPPs. These thin metallic wires contribute to the elimination of the TM_{10} mode and accumulation of electric charges to sustain the normal components of the electric field to face opposite each other at the interface. They also set an infinite small dipole vertical to the interface to excite the ESPPs. In this work, we show how these metallic wires at the interface between two different positive dielectrics contribute to the realization of ESPPs and study how the periodicity of the metallic wires affect the dispersion relations of the ESPPs.

III. REALIZATION AND SIMULATIONS

In this section, we first study the evolution of the dispersion relations of the TE_{10} modal-dispersion-induced ESPPs with variations of the periodicity of the metallic wires from $d = a/40$ to $d = a/10$ by using the eigenmode solver in the commercial software CST STUDIO and setting the boundary conditions in the x and y directions as the PEC and the z direction as the periodic boundary. It is obvious from Fig. 3 that when $d = a/40$, the simulated dispersion curve agrees with the analytical dispersion curve quite well. With the increase of d, the cutoff frequency and

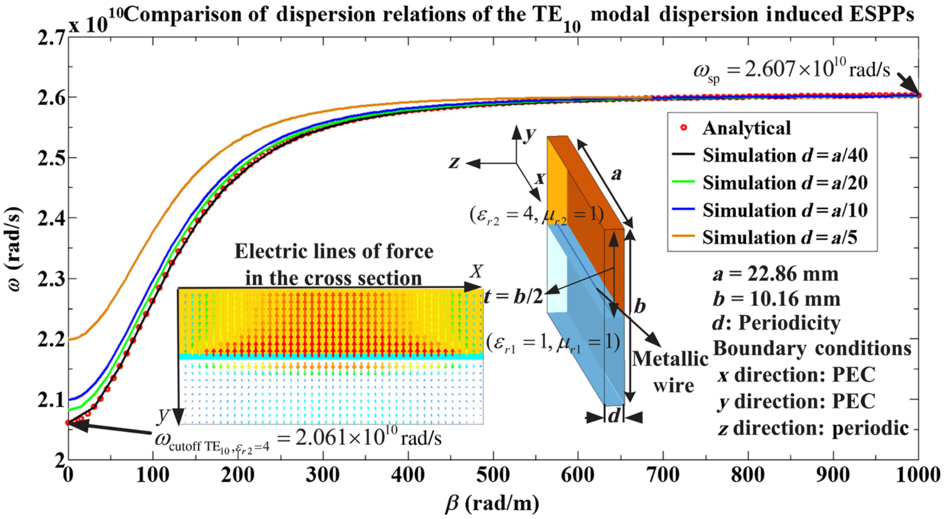

FIG. 3. Comparison of the analytical dispersion relations of the TE_{10} modal-dispersion-induced ESPPs with four simulated dispersion relations of different periodicities $d = a/40$, $d = a/20$, $d = a/10$, and $d = a/5$.

the dispersion curve deviate away from the analytical one. However, the asymptotic frequency does not change with different periodicities. The electric lines of force in the cross section are also drawn as the inset in Fig. 3, showing that the periodic metallic wires can accumulate electric charges to sustain the normal components of the electric field to face opposite each other at the interface. In addition, surface-confined modes cannot be supported merely at the interface between two positive dielectric layers in the waveguide without the metallic wires. Thus, all these features demonstrate that the periodic metallic wires play a key role in the excitations of the ESPPs, and the periodicity as small as $d = a/40$ can be chosen to realize the theoretical modal-dispersion-induced ESPPs.

Now we show in Fig. 4 how to realize smooth mode conversion between the TE_{m0}^z modes and the ESPPs with wave-port excitations instead of an electric dipole. The two regions with length $l_1 = l_5 = a$ in Fig. 4(a) are purely filled with the dielectric of relative permittivity $\varepsilon_{r2} = 4$, which is used as the input and output regions. The middle segment in the middle region is of height $h = b - t = b/2$, and the two side segments are mode-conversion regions with continuously increasing height of 0 up to h and decreasing height of h down to 0. A series of thin metallic wires of radius $r = a/200$ and distance $d = a/40$ are placed along the entire interface between the blue and brown regions. The input port (port 1) is excited with the dominant TE_{10}^z waves, and the output port (port 2) is set to receive the TE_{10}^z waves. It is expected that the ESPPs spectrum for this waveguide is 3.28 GHz $< f_0 <$ 4.15 GHz according to the above theory. The S-parameter spectrum from 2 to 6 GHz in Fig. 4(e) is obtained using the commercial software CST STUDIO, from which we can clearly observe that there exists a passband between 3.28 and 4.1 GHz. This passband agrees quite well with the theoretical predictions of the ESPPs spectrum, in which we pick up an arbitrary frequency point $f_0 = 3.8$ GHz and calculate the relative effective permittivities of these two dielectrics as $\varepsilon_{e1} = -1.98$ and $\varepsilon_{e2} = 1.02$. The electric lines of force and the y component of the electric field distributions in the y-$z(x = 0)$ and x-$z(y = b/2)$ planes at 3.8 GHz are shown in Figs. 4(b)–4(d), from which we can see that the TE_{10}^z waves excited at port 1 are gradually converted into the ESPPs in the middle region and converted back into TE_{10}^z waves at port 2. The field confinement level of the ESPPs in the middle is manifest higher than that of the TE_{10}^z waves on both sides. The wavelength of the ESPPs from the simulation results 41.76 mm $(0.529\lambda_0)$ agrees quite well with the theoretical predictions $\lambda_{\text{ESPPs},3.8\text{ GHz}} = 2\pi/\beta =$ 41.88 mm $(0.530\lambda_0)$ obtained from the analytical dispersion curve, in which λ_0 is the free-space wavelength according to the operating frequency $f_0 = 3.8$ GHz. We remark that in this whole ESPPs spectrum, the TE_{10}^z waves can be successfully converted into the ESPPs, and with the increase of f_0, the wavelength of the ESPPs is dramatically shortened and the field confinement level significantly enhances. In addition, the interface position can be chosen arbitrarily by tuning the thickness t of layer II, and the negative group velocity can be clearly observed by setting $b/2 < t < b$. This negative group velocity may arise with the strong coupling between the ESPPs in regions I and II when region I (the air) is thin enough, which is analogous to the negative group velocity of natural SPPs propagating in a thin metal film bounded by dielectrics.

Based on the same idea and under the same framework, two independent ESPPs channels can be constructed at $x = -(a/4)$ and $x = (a/4)$ two cross sections normal to the x direction under the excitation of the TE_{20}^z mode. To excite the TE_{20}^z mode, we can drive two probes spaced 1/4 and 3/4 of the way across the broad face in antiphase. When only the TE_{20}^z mode is considered in an X-band rectangular waveguide, the dispersion relation for the TE_{20}^z modal-dispersion-induced ESPPs at the interface between air $(\varepsilon_{r1} = 1)$ and a conventional nonmagnetic dielectric with relative permittivity $(\varepsilon_{2r} = 4)$ is

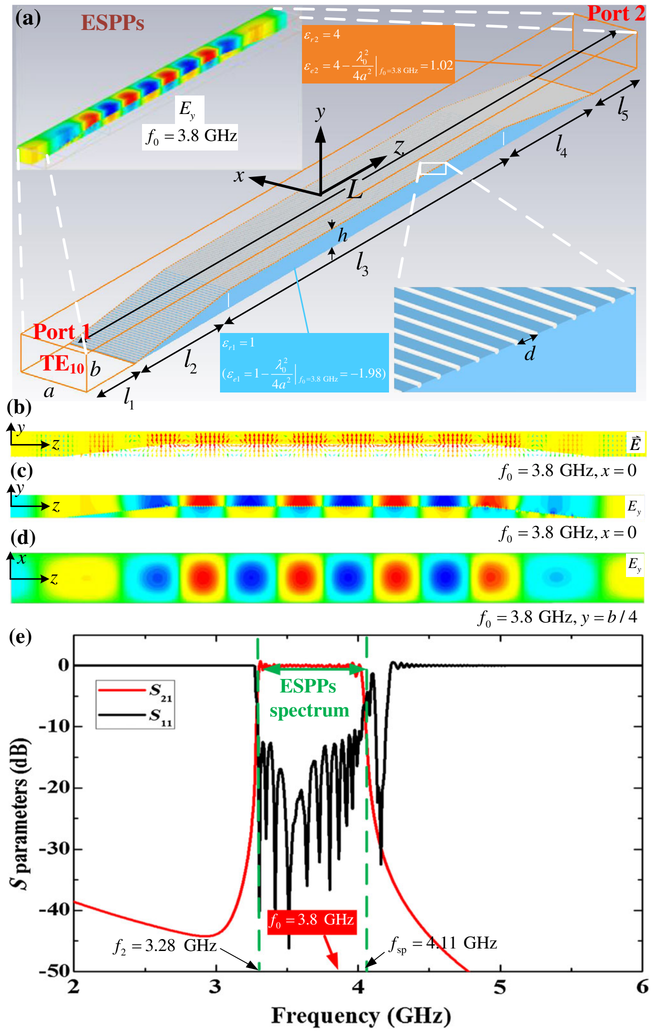

FIG. 4. Simulation of the TE$_{10}$ modal-dispersion-induced ESPPs in a standard X-band rectangular waveguide (WR90) with cross-section dimensions $a \times b = 22.86 \times 10.16$ mm^2 and length $L = 12a$. The brown region in the guide is filled with a dielectric of relative permittivity $\varepsilon_{r2} = 4$, and the light blue region is filled with air of $\varepsilon_{r1} = 1$, in which $l_2 = 2a$, $l_3 = 6a$, and $l_4 = l_2$. (a) Structure of the interface. (b) Distributions of electric force of lines on the y-z plane. (c) Distributions of E_y on the y-z plane. (d) Distributions of E_y on the x-z plane. (e) ESPPs spectrum.

$$\left[\omega^2 - c^2\left(\frac{2\pi}{a}\right)^2\right]\sqrt{\beta^2+\left(\frac{2\pi}{a}\right)^2-4k_0^2} \times \tanh\left[t\sqrt{\beta^2+\left(\frac{2\pi}{a}\right)^2-4k_0^2}\right] = -\left[4\omega^2 - c^2\left(\frac{2\pi}{a}\right)^2\right]\sqrt{\beta^2+\left(\frac{2\pi}{a}\right)^2-k_0^2} \times \tanh\left[(b-t)\sqrt{\beta^2+\left(\frac{2\pi}{a}\right)^2-k_0^2}\right]. \tag{3}$$

The evolution of the dispersion relations of the TE$_{20}^z$ modal-dispersion-induced ESPPs with variations of t can also be obtained by solving the transcendental equation, Eq. (3), numerically and shown in Fig. 2(b), which shows nearly the same manner as those of the TE$_{10}^z$ modal-dispersion-induced ESPPs in Fig. 2(a). This TE$_{20}^z$ modal-dispersion-induced ESPPs spectrum $[(\pi c)/a] = \omega_{\mathrm{cutoff\,TE}_{20},\varepsilon_{r2}=4} < \omega_0 < \omega_{\mathrm{SP}} = [(4\pi c)/\sqrt{10}a]$ can also be obtained. In addition, we can smoothly convert the TE$_{20}^z$ mode in a purely dielectric filled waveguide to the ESPPs at the dielectric-air interface between two equal-thickness layers simply by changing the thickness t from $t = b$ to $t = b/2$ continuously. With the same structure in Fig. 5(a), we calculate the S-parameter spectrum from 4 to 10 GHz and find a passband between 6.58 and 8.1 GHz shown in Fig. 5(d), which matches the analytical ESPPs spectrum 6.6 GHz $< f_0 <$ 8.15 GHz quite well. We draw the electric field E_y distributions at an arbitrary intraband

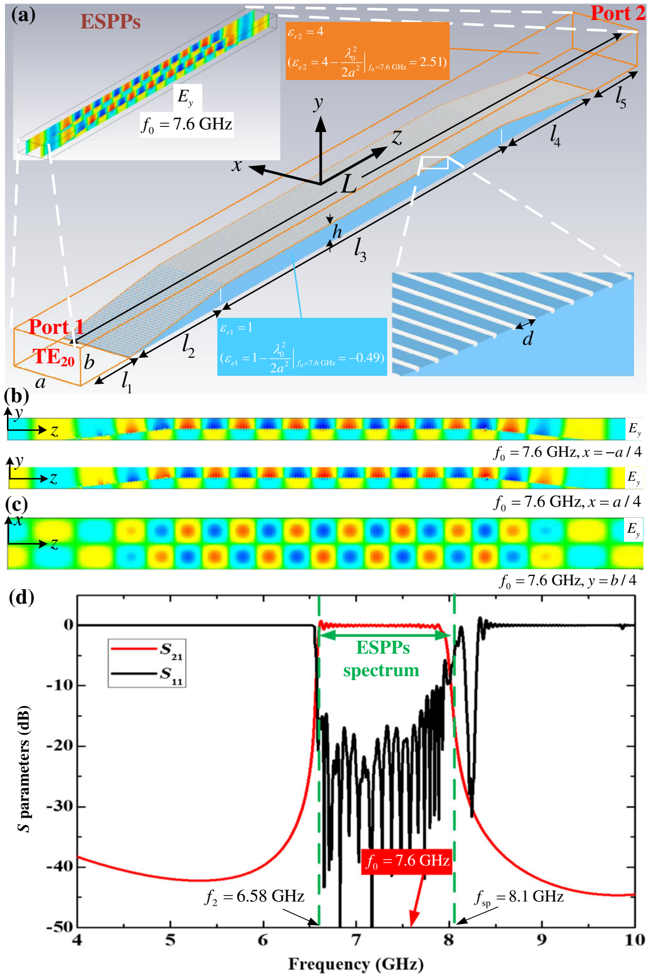

FIG. 5. Simulation of the TE$_{20}^z$ modal-dispersion-induced ESPPs in the same waveguide as that in Fig. 4(a). (a) Structure of the interface. (b) Distributions of E_y on the y-z plane. (c) Distributions of E_y on the x-z plane. (d) ESPPs spectrum.

frequency point $f_0 = 7.6$ GHz in two y-z planes at $x = -(a/4)$ and $x = (a/4)$ and one x-z plane at $y = (b/4)$ in Figs. 5(b) and 5(c), respectively. Two independent ESPPs channels centered at $x = -(a/4)$ and $x = (a/4)$ are clearly observed and out of phase due to the antiphase excitations of the TE_{20}^{z} mode. The corresponding relative effective permittivities of the two dielectrics for the TE_{20}^{z} mode at 7.6 GHz can be calculated as $\varepsilon_{e1} = -0.49$ and $\varepsilon_{e2} = 2.51$. The wavelength of the TE_{20}^{z} modal-induced ESPPs from the simulation results 23.41 mm $(0.593\lambda_0)$ agrees quite well with the theoretical predictions $\lambda_{\mathrm{ESPPs},7.6\ \mathrm{GHz}} = 2\pi/\beta = 23.44$ mm $(0.594\lambda_0)$ obtained from the analytical dispersion curve, in which λ_0 is the free-space wavelength at the operating frequency 7.6 GHz.

Thus, it is natural to expect that the ESPPs can also be supported at the same interface under the TE_{m0}^{z} mode excitations in the frequency range $[mc/(2a\sqrt{\varepsilon_r})] < f_0 < [mc/(\sqrt{2}a\sqrt{1+\varepsilon_r})]$, $m \geq 3$. In addition, m ESPPs channels can be found across the broad face with two adjacent channels being out of phase.

IV. EXPERIMENTS AND DISCUSSION

Although the above theoretical analysis is based on the rectangular waveguide, it can be reasonably and easily transferred to its planarized counterpart, the substrate-integrated waveguide. Thus, for the ease of fabrication and testing, in this section, a double-layered SIW shown in Fig. 6 is judiciously designed to support the ESPPs at the interface between these two layers. A sticking dielectric layer is placed between layer I and layer II according to the fabrication requirements. The dielectrics of layer I (top layer), layer II (bottom layer), and the sticking layer in between are Rogers RO4350B with permittivity $\varepsilon_r = 3.48$ and loss angle tangent $\tan\delta = 0.0037$ and designed with thicknesses of 0.762, 0.338, and 0.1 mm, respectively. All the metal layers are made with copper of thickness 0.018 mm. Two rows of vias are dug through from the top layer to the bottom layer, forming a two-layered SIW in the middle connected with two microstrip-to-SIW transitions on both sides. All the specific dimensions are listed in Fig. 6 in units of millimeters. A rectangular air slot of dimension $20 \times 15\ \mathrm{mm}^2$ is formed by digging through the dielectrics of the sticking layer and layer II. The width of the air slot is chosen as 15 mm, which is relatively smaller than the distance 19 mm between the two vias in the y direction to avoid the damage to the vias when fabricated. A series of ultrathin copper wires with dimensions $0.1 \times 19\ \mathrm{mm}^2$ are placed at the back of the dielectric of layer I, which act as the ESPPs interface between the dielectric region in layer I and the air region in the sticking layer and layer II. No transition region is built considering that the thickness of each layer is too thin. According to the above theory, the ESPPs spectrum can be calculated with the width of the SIW $a = 20$ mm, height $b = 1.2$ mm, and dielectric thickness $t = 0.762$ mm based on Eq. (2) as 4.25 GHz $< f_0 <$ 5.52 GHz. The electric fields E_y at 5.2 GHz in layers I (dielectric layer) and II (air-slot layer) are simulated and shown in Figs. 7(c) and 7(d), in which we can clearly observe that the electric fields are out of phase in the ESPPs regions. In addition, the wavelength of the ESPPs is shortened, and the electric field density is relatively higher compared with the TE_{10} mode in the SIW region on both sides.

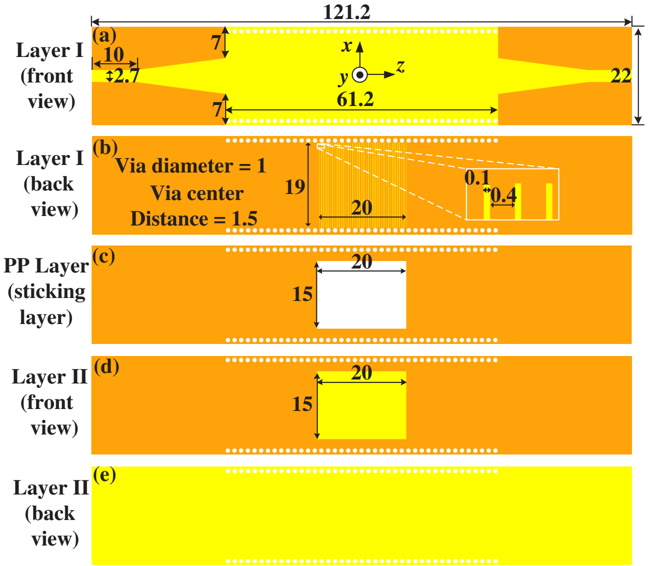

FIG. 6. Schematic drawing of each layer in the double-layered SIW for the transmission of ESPPs. All the numbers are in units of millimeters. (a) Front view of layer I. (b) Back view of layer I. (c) Sticking layer. (d) Front view of layer II. (e) Back view of layer II.

We fabricate a real sample with the front and back views shown in Figs. 7(a) and 7(b). The metal layer covering the air slot on the back side is deliberately cut off to give a better inner view inside the air slot. The two ports are connected to the test cables of an N5230C vector network analyzer through SMA connectors. The S parameters are tested and shown in Fig. 7(e), where we can clearly observe that the experimental results agree quite well with the simulated ones for both the S_{21} and S_{11} spectra between 3 and 6 GHz. The discrepancies between the simulation and experimental results may come from the material and fabrication tolerances. The pass band between 4.3 and 5.48 GHz is actually the ESPPs spectrum. The discrepancy between the experimental results and theoretical predictions comes from the inconsistency between the fabrication and theoretical models due to the fabrication requirement that the air-slot region does not cover the whole width of the SIW. However, both the simulated electric field distributions and the tested S parameters demonstrate that the ESPPs are generated and transmitted on this ultrathin SIW platform. Furthermore, the group delay of the waveguide in the frequency range 4.2 GHz $< f_0 <$ 5.6 GHz is tested

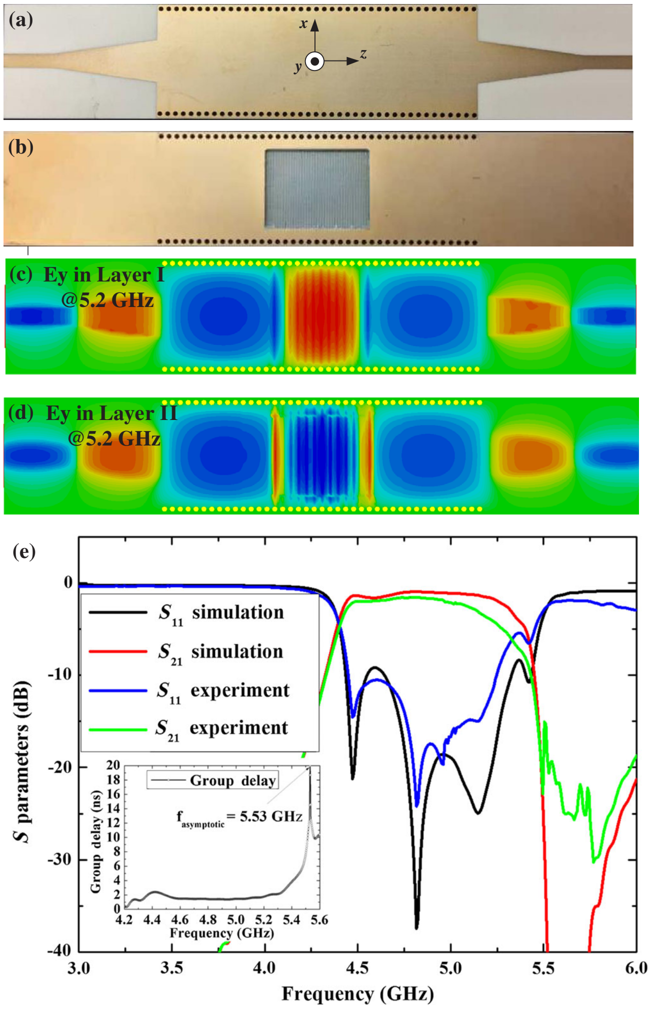

FIG. 7. ESPPs in a real fabricated sample of the double-layered SIW and the ESPPs spectrum. (a) Front view. (b) Back view. (c) Simulated E_y distributions in layer I at 5.2 GHz. (d) Simulated E_y distributions in layer II at 5.2 GHz. (e) ESPPs spectrum obtained in the simulations and experiments.

and shown as the inset of Fig. 7(e). We can clearly observe that in the ESPPs spectrum, the group delay increases from about 2 to nearly 20 ns, which means that the waves propagate very slowly near the asymptotic frequency of the ESPPs and demonstrates the slow-wave properties of the ESPPs.

In addition to the TE^z_{m0} modes, other TE^z_{mn} or TE^z_{mn} modes in the rectangular waveguide can also possibly be used to induce the corresponding ESPPs pertaining to that mode with specific design if the electric and magnetic field force of lines of that mode meet the requirement of natural SPPs. For instance, the TE^z_{01} mode is very much like the TE^z_{10} mode with only the electric field normal to the narrow face instead of the broad face of the rectangular waveguide; thus, it is a simple route to construct an interface with the normal being perpendicular to that of the TE^z_{10} case. Very similar ESPPs corresponding to the TE^z_{01} mode are observed and not shown here without affecting the integrity of this work. Moreover, we can see from the relative effective permittivity formula that both ε_{e1} and ε_{e2} are frequency dependent, which is quite different from natural SPPs excited at the interface between dielectric and metals in optical frequencies where the permittivity of the dielectric is nearly frequency independent within the observation spectrum. Therefore, the modal-dispersion-induced ESPPs are expected to be much more frequency sensitive and can be tuned by both the geometrical and medium parameters as well as the modes in the waveguide.

V. CONCLUSIONS

In summary, we dig into the origin of the modal-dispersion-induced effective SPPs at the interface between two positive dielectrics in the rectangular waveguide. The corresponding field distributions, dispersion relations, and asymptotic frequency are derived analytically and verified through simulations in two specific cases. An ultrathin double-layered SIW with an air slot and a series of metallic wires is demonstrated to support the ESPPs at the interface between two layers through experiments. The modal-dispersion-induced ESPPs differ from natural SPPs in several aspects, i.e., the dispersion relations, spectrum, and frequency sensitivity. This theory can be expected to be applied in circular waveguide, elliptical waveguide, substrate-integrated waveguide, and other bounded waveguides and may find potential applications in filters, resonators, and sensors of ESPPs in the microwave and low-terahertz frequencies.

ACKNOWLEDGMENTS

Z. L. acknowledges the financial support from Natural Science Foundation of Jiangsu Province under Grant No. BK20151480, Fundamental Research Funds for the Central Universities under Grant No. NS2016039, and the priority academic program development of Jiangsu Higher Education Institutions. Y. L. acknowledges the financial support from Singapore Ministry of Education Academic Research Fund TIER 1 under Grant No. RG72/15 and TIER 2 under Grant No. MOE2015-T2-1-145

[1] W. L. Barnes, A. Dereux, and T. W. Ebbesen, Surface plasmon subwavelength optics, Nature (London) **424**, 824 (2003).
[2] E. Ozbay, Plasmonics: Merging photonics and electronics at nanoscale dimensions, Science **311**, 189 (2006).
[3] T. W. Ebbesen, C. Genet, and S. I. Bozhevolnyi, Surface-plasmon circuitry, Phys. Today **61**, No. 5, 44 (2008).
[4] K. A. Willets and R. P. Van Duyne, Localized surface plasmon resonance spectroscopy and sensing, Annu. Rev. Phys. Chem. **58**, 267 (2007).

[5] N. Fang, H. Lee, C. Sun, and X. Zhang, Sub-diffraction-limited optical imaging with a silver superlens, Science **308**, 534 (2005).

[6] M. Ozaki, J. Kato, and S. Kawata, Surface-plasmon holography with white-light illumination, Science **332**, 218 (2011).

[7] P. Muhlschlegel, H. J. Eisler, O. J. Martin, B. Hecht, and D. W. Pohl, Resonant optical antennas, Science **308**, 1607 (2005).

[8] W. Y. Li, P. H. C. Camargo, X. M. Lu, and Y. N. Xia, Dimers of silver nanospheres: Facile synthesis and their use as hot spots for surface-enhanced Raman scattering, Nano Lett. **9**, 485 (2009).

[9] J. N. Anker, W. P. Hall, O. Lyandres, N. C. Shah, J. Zhao, and R. P. Van Duyne, Biosensing with plasmonic nanosensors, Nat. Mater. **7**, 442 (2008).

[10] J. B. Pendry, L. Martin-Moreno, and F. J. Garcia-Vidal, Mimicking surface plasmons with structured surfaces, Science **305**, 847 (2004).

[11] A. Pors, E. Moreno, L. Martin-Moreno, J. B. Pendry, and F. J. Garcia-Vidal, Localized Spoof Plasmons Arise while Texturing Closed Surfaces, Phys. Rev. Lett. **108**, 223905 (2012).

[12] A. P. Hibbins, B. R. Evans, and J. R. Sambles, Experimental verification of designer surface plasmons, Science **308**, 670 (2005).

[13] F. J. Garcia-Vidal, L. Martin-Moreno, and J. B. Pendry, Surfaces with holes in them: New plasmonic metamaterials, J. Opt. A **7**, S97 (2005).

[14] A. P. Hibbins, M. J. Lockyear, I. R. Hooper, and J. R. Sambles, Waveguide Arrays as Plasmonic Metamaterials: Transmission below Cutoff, Phys. Rev. Lett. **96**, 073904 (2006).

[15] Y. J. Zhou, Q. Jiang, and T. J. Cui, Bidirectional bending splitter of designer surface plasmons, Appl. Phys. Lett. **99**, 111904 (2011).

[16] X. Gao, J. H. Shi, X. Shen, H. F. Ma, W. X. Jiang, L. Li, and T. Cui, Ultrathin dual-band surface plasmonic polariton waveguide and frequency splitter in microwave frequencies, Appl. Phys. Lett. **102**, 151912 (2013).

[17] X. Shen and T. J. Cui, Planar plasmonic metamaterial on a thin film with nearly zero thickness, Appl. Phys. Lett. **102**, 211909 (2013).

[18] Z. Li, L. Liu, C. Gu, P. Ning, B. Xu, Z. Niu, and Y. Zhao, Multi-band localized spoof plasmons with texturing closed surfaces, Appl. Phys. Lett. **104**, 101603 (2014).

[19] Z. Li, B. Xu, C. Gu, P. Ning, L. Liu, Z. Niu, and Y. Zhao, Localized spoof plasmons in closed textured cavities, Appl. Phys. Lett. **104**, 251601 (2014).

[20] Z. Liao, X. Shen, B. C. Pan, J. Zhao, Y. Luo, and T. J. Cui, Combined system for efficient excitation and capture of LSP resonances and flexible control of SPP transmissions, ACS Photonics **2**, 738 (2015).

[21] T. Jiang, L. Shen, X. Zhang, and L. Ran, High-order modes of spoof surface plasmon polaritons on periodically corrugated metal surfaces, Prog. Electromagn. Res. M **8**, 91 (2009).

[22] X. Zhang, L. Shen, and L. Ran, Low-frequency surface plasmon polaritons propagating along a metal film with periodic cut-through slits in symmetric or asymmetric environments, J. Appl. Phys. **105**, 013704 (2009).

[23] Z. Liao, Y. Luo, A. I. Fernández-Domínguez, X. Shen, S. A. Maier, and T. J. Cui, High-order localized spoof surface plasmon resonances and experimental verifications, Sci. Rep. **5**, 9590 (2015).

[24] Z. Gao, L. Shen, J. J. Wu, T. J. Yang, and X. Zheng, Terahertz surface plasmon polaritons in textured metal surfaces formed by square arrays of metallic pillars, Opt. Commun. **285**, 2076 (2012).

[25] S. J. Berry, T. Campbell, A. P. Hibbins, and J. R. Sambles, Surface wave resonances supported on a square array of square metallic pillars, Appl. Phys. Lett. **100**, 101107 (2012).

[26] B. J. Yang, Y. J. Zhou, and Q. X. Xiao, Spoof localized surface plasmons in corrugated ring structures excited by microstrip line, Opt. Express **23**, 21434 (2015).

[27] S. Kim, S. Oh, K. Kim, J. Kim, H. Park, W. Hess, and C. Kee, Subwavelength localization and toroidal dipole moment of spoof surface plasmon polaritons, Phys. Rev. B **91**, 035116 (2015).

[28] F. Gao, Z. Gao, X. H. Shi, Z. J. Yang, X. Lin, H. Y. Xu, J. D. Joannopoulos, M. Soljačić, H. S. Chen, L. Lu, Y. D. Chong, and B. L. Zhang, Probing topological protection using a designer surface plasmon structure, Nat. Commun. **7**, 11619 (2016).

[29] R. J. Li, M. Imran, X. Lin, H. P. Wang, Z. W. Xu, and H. S. Chen, Hybrid Airy plasmons with dynamically steerable trajectories, Nanoscale **9**, 1449 (2017).

[30] X. Lin, I. Kaminer, X. H. Shi, F. Gao, Z. J. Yang, Z. Gao, H. Buljan, J. D. Joannopoulos, M. Soljačić, H. S. Chen, and B. L. Zhang, Splashing transients of 2D plasmons launched by swift electrons, Sci. Adv. **3**, e1601192 (2017).

[31] C. D. Giovampaola and N. Engheta, Plasmonics without negative dielectrics, Phys. Rev. B **93**, 195152 (2016).